Journal of Colloid and Interface Science 723 (2026) 140912

Contents lists available at ScienceDirect

Journal of Colloid And Interface Science

journal homepage: www.elsevier.com/locate/jcis

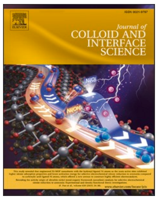

Mechanical reinforcement of gellan–alginate hydrogels using commercial functionalized silica particles and mild surface chemistry

Juan Pablo Segovia-Gutiérrez [a], José Alberto Rodríguez Agudo [b], Sönke Wengler-Rust [b], Nicolas Binder [b], Peter Georg Weidler [c], Frank Kirschhöfer [c], Jürgen Utz [b], Natalie Germann [a,*]

[a] Institute of Process Systems Engineering, University of Stuttgart, Böblinger Str. 78, 70199 Stuttgart, Germany
[b] Anton Paar Germany GmbH, Hellmuth-Hirth-Strasse 6, 73760 Ostfildern-Scharnhausen, Germany
[c] Institute of Functional Interfaces, Karlsruhe Institute of Technology, Hermann-von-Helmholtz-Platz 1, 76344 Eggenstein-Leopoldshafen, Germany

GRAPHICAL ABSTRACT

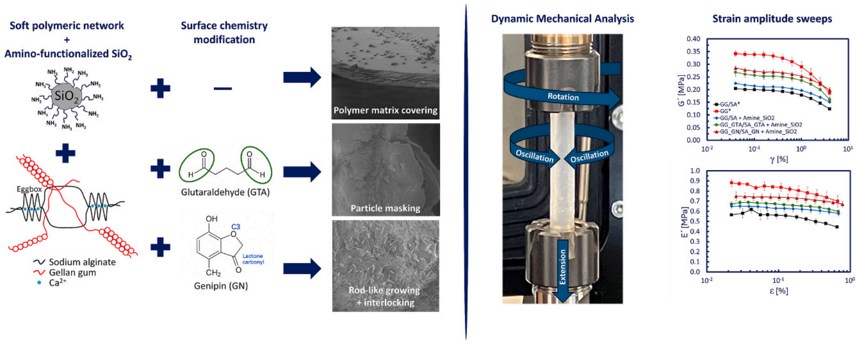

ARTICLE INFO

Keywords:
Mesoporous silica particles
Soft polymeric network
Glutaraldehyde
Genipin
Surface chemistry
Dynamic mechanical analysis

ABSTRACT

Hydrogels offer tunable mechanical properties that can be enhanced through tailored polymer–colloidal filler interactions. This work examines the interfacial behavior in gellan gum/sodium alginate soft polymeric networks reinforced with commercial polydisperse amine-functionalized mesoporous silica particles, and glutaraldehyde (GTA) or genipin (GN) as bifunctional surface activators. The reinforcement mechanism was elucidated through quantitative in-line pH kinetics and surface charge evolution analysis. A critical 'electrostatic window' was identified where the surface charge of the amino-functionalized silica transitions from +20.9 mV to −11.5 mV, minimizing particle–polymer repulsion and facilitating interfacial anchoring. Furthermore, particle-size heterogeneity was found to broaden the linear viscoelastic regime by creating a distributed, particle-bridged interfacial network. Surface activation by GTA or GN introduced additional stiffening. While both activators reduce surface charge, GN produced the largest mechanical enhancement due to its slower, more controlled reaction pathway. Scanning electron microscopy (SEM) revealed the growth of rod-like structures at the particle-polymer interface in GN-activated systems, providing a physical interlocking mechanism that substantiates the observed 15% increase in storage modulus, *G'*. While FT-IR detected only subtle chemical changes, X-ray

---

* Corresponding author.
E-mail addresses: juanpablo.segovia@svt.uni-stuttgart.de (J.P. Segovia-Gutiérrez), jose.rodriguez@anton-paar.com (J.A.R. Agudo), soenke.wengler-rust@anton-paar.com (S. Wengler-Rust), nicolas.binder@anton-paar.com (N. Binder), peter.weidler@kit.edu (P.G. Weidler), frank.kirschhoefer@kit.edu (F. Kirschhöfer), juergen.utz@anton-paar.com (J. Utz), natalie.germann@svt.uni-stuttgart.de (N. Germann).

https://doi.org/10.1016/j.jcis.2026.140912
Received 23 February 2026; Received in revised form 15 May 2026; Accepted 8 June 2026

diffraction revealed a significant shift in the amorphous silica reflection from 23° to 13°, indicating structural rearrangements consistent with covalent interfacial coupling. These results demonstrate that synchronizing reaction kinetics with the electrostatic landscape provides a data-backed strategy to optimize the robustness of hybrid polymeric networks.

1. Introduction

Hydrogels are mechanically stable, three-dimensional soft polymeric networks characterized by high water content and a predominant elastic response within the linear viscoelastic region [1]. Their structural capacity to withstand and recover from deformation makes them suitable candidates for advanced applications, including soft electronics [2,3], biomedicine [4–7], wearable sensors [8], and optics [9].

A primary challenge in the development of these materials is the precise tuning of their mechanical performance. The integration of colloidal particles into the polymer matrix represents a conventional strategy for mechanical reinforcement, where the viscoelastic moduli are governed by particle-network interactions and interparticle forces. This reinforcement is driven by size-dependent effects, as described, for instance, in the case of PAAM hydrogels with silica inclusions. The elastic modulus rapidly increases when the particle size decreases toward the nanometer scale, however no relevant changes in the modulus are observed when particles are within the micrometer range [10]. In blends of soft polymer colloids, specifically latex, and calcium carbonate powders of different sizes as fillers, the mechanical reinforcement was improved for lower filler:polymer ratios, i.e. smaller filler sizes. However, fillers at the nanoscale also introduced more brittleness to the blend [11].

The particle size distribution is also a critical determinant of the final rheological profile. For instance, the transition from larger, polydisperse fillers to smaller particles with narrow size distributions has been shown to provide significantly stronger reinforcement of the storage modulus [12]. Parallel to particle size and particle size distribution, the volume fraction is also a critical parameter. At intermediate particle volume fractions, increasing polymer concentration favors depletion attraction between particles, driving a structural transition from a liquid of colloidal clusters to a heterogeneous, space-spanning colloidal gel network. This transition shifts the rheological response from diffusion-based relaxation to a solid-like state where the elastic modulus increases linearly with attraction strength [13]. This suggests that the mechanical properties can be systematically engineered by controlling the colloidal assembly and the range of particle-particle interactions within the aqueous environment of the gel.

While suggested mechanical improvements are driven by particle sizes and particle volume fractions, the reinforcing mechanisms can be further refined at the individual colloidal level, for instance, by introducing electrostatic interactions. These interactions can occur at the particle-polymer interface, and can be modulated to facilitate robust particle-polymer linkages to reinforce the mechanical behavior [14], or to introduce new advanced features such as the self-healing abilities [15]. But electrostatic interactions play also a fundamental role when particle-particle assemblies are considered contributing, for example, in the creation of stable space-spanning networks to build colloidal gels [16]. Another conventional route to induce reinforcement at the colloidal level is to introduce particle-polymer covalent bonds, as demonstrated for ethylene-octene copolymer and nanosilica composites [17].

The majority of existing research focuses on reinforcement within medium to high particle volume fractions, where even electrostatic and covalent interactions are typically analyzed at volume fractions that allow colloidal space-spanning networks. However, the mechanical behavior of these systems in the dilute regime remains poorly understood, particularly regarding the synchronization between surface reaction kinetics and the electrostatic landscape. While structural integrity is influenced by localized electrostatic interactions, the transition from purely physical association to covalent interfacial anchoring requires precise timing between the polymer gelation and the particle surface activation. Without a quantitative characterization of this interfacial evolution, the underlying mechanism for synergistic reinforcement remains speculative. This transition aligns with recent findings on the modulation of electrostatic interactions between fillers and polymer chains [18], yet the potential for chemical activation in these dilute systems remains untapped. To address this, a part of this work introduces an alternative application for glutaraldehyde (GTA) and genipin (GN). Rather than their traditional role as bulk polymer crosslinkers, we utilize them as surface activator agents.

GTA is a synthetic compound widely used as a crosslinker in the hydrogel field, owing to its effectiveness in covalent crosslinking that stems from its rapid and efficient reaction kinetics [19] via Schiff base formation. GTA is often used with chitosan, for example, in double network hydrogels where chitosan is covalently crosslinked with GTA, while sodium alginate (SA) is physically crosslinked by Ca^{2+} ions [20]. Although GTA is an effective crosslinker, it also presents cytotoxicity [21], limiting its use in biomedicine or in applications requiring contact with living tissue. The natural compound GN is also used in hydrogel syntheses as a crosslinker. Compared with GTA, GN exhibits slower reaction kinetics due to its multistep reaction, which involves ring opening followed by the formation of a secondary amine. However, GN has low cytotoxicity [22] and has emerged as a viable alternative to GTA. GN is commonly combined with chitosan [23] for biomedical and pharmaceutical applications, and it is also utilized in hydrogel composites for tissue engineering [24].

The application of GTA or GN generally relies on the presence of amino groups at the particle-polymer or polymer-polymer interface. Consequently, their use is typically confined to polymers that naturally carry amino functionalities or must undergo prior chemical modification, as is the case for gellan gum (GG) and SA. In this work, we investigate the mechanical reinforcement of GG/SA hydrogels by quantifying the relationship between surface reaction kinetics and electrostatic evolution at the particle-polymer interface. By integrating real-time inline pH monitoring with Zeta potential analysis, we move beyond qualitative observations to provide an empirical basis for the interfacial anchoring mechanism. Finally, we employ scanning electron microscopy (SEM) and X-ray diffraction (XRD) to probe the resulting network microstructures. As will be shown, these investigations revealed the unexpected formation of rod-like structures at the interface (Fig. 1), providing a physical basis for the observed viscoelastic stability and offering a data-backed strategy for optimizing hybrid hydrogel robustness.

2. Materials and methods

2.1. Materials

Glucono-δ-lactone (GDL, Cat. No. G2164-100G), mesoporous MCM-48 particles (< 15 μm particle size, pore size 3 nm, amine-functionalized, Cat. No. 900769-5G), and GTA in 50% aqueous solution (GTA, $M_w = 100.12$ g/mol, Cat. No. 340855-25ML) were supplied by Merck. GN in powder form (GN, $M_w = 226.23$ g/mol, Cat. No. OR932863-5G) was purchased from Apollo Scientific, and its solvent dimethyl sulfoxide (DMSO, Cat. No. A3672.0100) was supplied by PanReac AppliChem. Calcium carbonate ($CaCO_3$, Cat. No. 33295) and gellan gum (GG, Cat. No. J63423.30, $M_w = 1.83 \pm 0.07 \times 10^6$ Da) were purchased from Thermo Scientific. Sodium alginate (SA, Cat. No. A3249,0250, $M_w = 6.105 \pm 0.007 \times 10^5$ Da), with high guluronic acid (G) residue content and a corresponding mannuronic-to-guluronic acid (M/G) ratio of 1.38, was supplied by PanReac AppliChem [25]. GG and SA came from the same lots used in our previous publication, where Gel Permeation Chromatography (GPC) experiments were carried out to estimate their corresponding molecular weights [26].

2.1.1. *Preparation of unfilled hydrogels*

The preparation procedure followed the steps described in our previous publication [26]. The corresponding amounts of the different chemicals were selected to prepare 100 ml batches. Into a 150 ml borosilicate beaker (VWR), 90 ml of Milli-Q water was poured and then heated to 80 °C using a magnetic stirring heating plate (VWR Advanced VMS-C7). At a constant temperature (*T*) of 80 °C, a total concentration of 2% (*w/v*) polymers was added. For the hydrogel composed of GG and SA, the ratio was 8:2. For the pure GG, the ratio was 10:0. The beaker was sealed with a plastic sealing film (Seal-R-film™) to retain evaporated water. After 3 h of moderate continuous stirring to ensure complete hydration of the polymers, *T* was set to 50 °C. The addition of GDL and $CaCO_3$ was as follows: 0.5 g of GDL was dissolved in 5 ml of Milli-Q water, and 0.3 g of $CaCO_3$ was dispersed in 5 ml of Milli-Q water. The 5 ml GDL solution was poured into the polymer solution, and the mixture was vigorously stirred. Then, the 5 ml $CaCO_3$ dispersion was added to it and stirred vigorously again. After 30 min, the sample was cooled to room temperature (*RT*) to reach the final gel state. The hydrogels were stored in a refrigerator until measurements were performed.

2.1.2. *Preparation of hydrogel filled with particles*

Filled hydrogels, without GTA or GN, were prepared by incorporating amine-functionalized mesoporous silica particles (0.7% (w/v) final content) into the polymer solution [26]. The particles were first dispersed in 4 ml of Milli-Q water using an ultrasonic bath at low power until visible aggregates disappeared. The dispersion was added to the fully dissolved polymers in water at 80 °C and magnetically stirred until homogenization. The mixture was cooled down to 50 °C, and a 3 ml GDL solution and a 3 ml $CaCO_3$ dispersion were added following the procedure described above. After 30 min, the sample was again cooled to *RT* to reach the final gel state. Hydrogels were then stored in a refrigerator until use.

The synthesis of filled hydrogels including GTA is described in the following. Prior to the addition of GDL and $CaCO_3$, with the particle-polymer suspension at 50 °C, 217 μl of the 50% GTA solution, equivalent to 0.12 g of pure GTA, was poured into the mixture. The chemical reaction was maintained for 1.5 h, resulting in the characteristic yellowish coloration (Fig. 3a) of GTA reactions [27]. Then, the 5 ml GDL solution and the 5 ml $CaCO_3$ dispersion were added as previously described. After 30 min, the sample was cooled to *RT* and stored in a refrigerator.

Filled hydrogels including GN were synthesized as follows. First, 0.27 g of GN was dissolved in 6 ml of DMSO in a vial. DMSO was used due to the low solubility of GN in water. To match the final volume of 100 ml, the polymers were dissolved in 84 ml of Milli-Q water at 80 °C. Then, the 4 ml particle suspension was added to the solution at 80 °C. The mixture was cooled to 50 °C, and the GN-DMSO solution was subsequently poured in. The chemical reaction was maintained for 3 h, resulting in the typical dark blueish coloration observed in GN reactions, as shown in Fig. 3b. Then, the corresponding 3 ml GDL solution and 3 ml $CaCO_3$ dispersion were added. After 30 min, the sample was cooled to *RT* and stored in the refrigerator. Importantly, the amounts of GTA and GN were selected to ensure an excess number of molecules available to interact with the amino groups on the particle surface. The surface density of amino groups was assumed to be 1 group/nm^2 [28].

2.1.3. *Sample preparation for Fourier-transform infrared (FT-IR) spectroscopy*

Cylindrical cutouts of 1 cm diameter were obtained from the hydrogel blocks. Using a cutter, the cylinders were manually cut into thin slices. These were then placed on a non-stick surface and dried at *RT* for 3 days. The dried slices were stored at *RT* in a low relative humid environment prior to measurements.

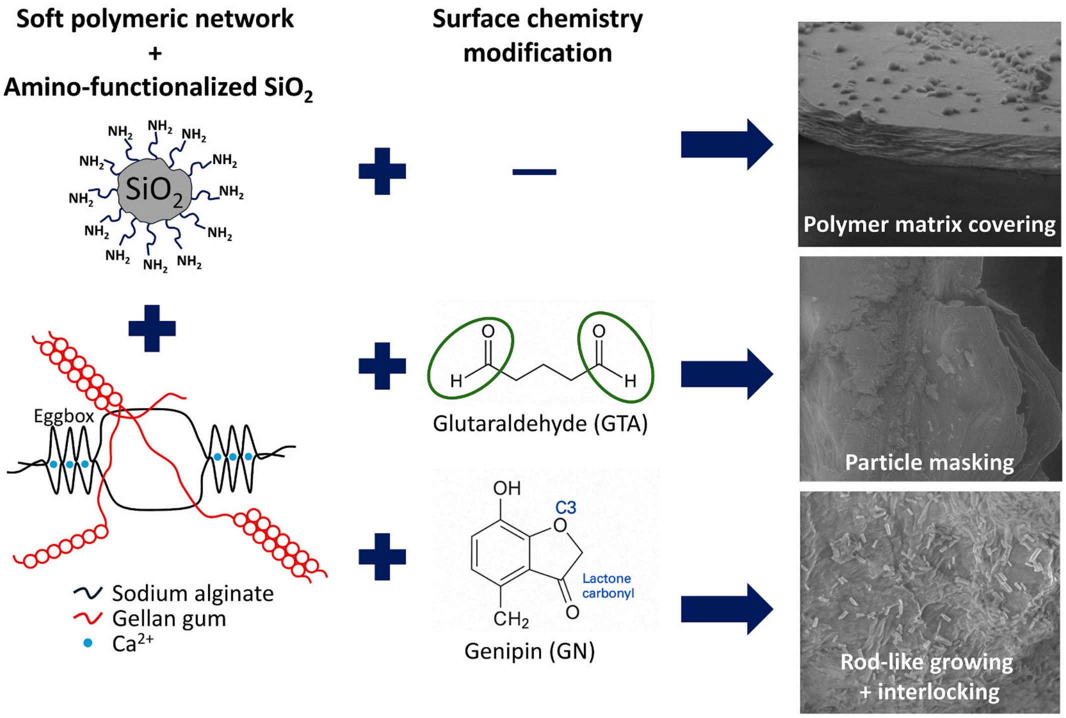

Fig. 1. Representation of the soft polymeric network with the typical “eggbox” structure of SA and plausible polymer-colloid interactions following the addition of GTA or GN.

2.1.4. Sample preparation for X-ray diffraction (XRD) analysis

Hydrogels were freshly prepared and pre-frozen for 4 h at −20 °C before lyophilization. The hydrogels were then placed in a dry freezer (Christ Alpha 1–4) preset at −54 °C. An external pump was used to apply a vacuum of 5×10^{-3} Torr. These conditions were maintained for at least 2 days to ensure complete lyophilization. A significant reduction in the original volume of the hydrogels was observed due to the absence of water, while the original shape was retained. Thin slices were cut from the dried samples (Fig. 2) and used in the XRD experiments.

2.1.5. Sample preparation for scanning electron microscopy (SEM)

Freeze-dried hydrogels prepared for XRD analysis were also used to performed SEM experiments. Small cutouts of the dry samples were placed onto carbon adhesive disks (no gold coatings were applied), transferred to the SEM, and evacuated directly to ESEM conditions (100 Pa chamber pressure, medium = water).

2.1.6. Sample preparation for zeta potential analysis

Three solutions at pH 5.14, 6.16, and 7.02 were prepared by combining an acetic acid/distilled water solution, and a sodium hydroxide/distilled water solution. The pH was monitored during the addition of small aliquots of the basic solution into the acidic solution until the desired pH was reached. Roughly 20 mg of the particles were dispersed in the solution of defined pH by ultrasonic treatment for 5 min. The particles were then filtered with a 5 μm cellulose acetate membrane filter, and transferred into an Omega cuvette (Anton Paar) for the measurement.

2.1.7. Sample preparation for in-line pH monitoring of the reactions

For pH monitoring prior to gelation, starting polymer solutions were prepared according to the protocol for filled hydrogels outlined in Subsection 2.1.2. However, direct pH monitoring during the gelation stage itself is unfeasible, as the transition from a liquid to a solid matrix interferes with sensor accuracy and risks damaging the probe. To circumvent this, the gelation process was simulated using standard acetic acid/sodium hydroxide buffer solutions. These buffers were calibrated to an initial pH matching that of the actual polymer precursors immediately before the addition of GDL and $CaCO_3$, enabling the precise measurement of the chemical environment while maintaining a liquid state.

2.2. Rheometric characterization

All experimental rheometric measurements were performed using an MCR 702e Space MultiDrive Rheometer (Anton Paar GmbH) with the necessary accessories. Hydrogel samples were cut into cylinders (Fig. 3c) with a length (*L*) and a diameter (*D*) of approximately 40 mm and 6.7 mm respectively and clamped in the geometry inside a CTD 180 temperature-humidity chamber (Fig. 3d). *T* was set at 30 °C, and the relative humidity (*RH*) was maintained at 90% to prevent rapid water loss from the hydrogel due to evaporation. The sample shape and environmental conditions were set to mimic the experimental conditions applied in our previous study [26]. The results presented are averages of at least three different measurements with fresh samples. The error bars correspond to the standard deviation. These general conditions always apply, unless specified otherwise.

2.2.1. Torsional-extensional dynamic mechanical tests (DMA)

The samples were subjected to dynamic extensional and torsional loadings. The specific *L*/*D* ratio was selected to ensure the estimated E' and E' were independent of the ratio itself. This offers a distinct advantage over classical parallel plate squeeze flow tests [29]. Additionally, cylindrical samples do not exhibit warping deformations due to torsion; hence, corrections of the complex shear modulus were unnecessary [30–36]. Therefore, the setup provided absolute values for torsional (G', G'') and extensional moduli (E', E'') in a continuous measurement run.

2.2.1.1. Amplitude sweeps. Amplitude sweeps in shear and extension modes were performed individually at a constant angular frequency of $\omega = 1$ rad/s. In shear mode tests, the shear strain varied from 0.01 to 1000%. For the extension mode, forces varied from 1 to 1000 mN. Results are shown in Fig. 8.

2.2.1.2. Frequency sweeps. Frequency sweeps were conducted in shear and extension modes during the same measurement run. The angular frequency sweeps were set to start at 100 rad/s and end at 1 rad/s. The sample was first subjected to shear mode with a constant shear strain of 0.1%, followed by extension mode with a constant strain force of 30 mN, equivalent to strain amplitudes between 0.1% and 0.15%. These amplitudes remain within the linear viscoelastic range during the experiment. Results are presented in Fig. 9.

2.2.2. Breaking rod tests

The tests were performed in torsion with an angular deformation rate

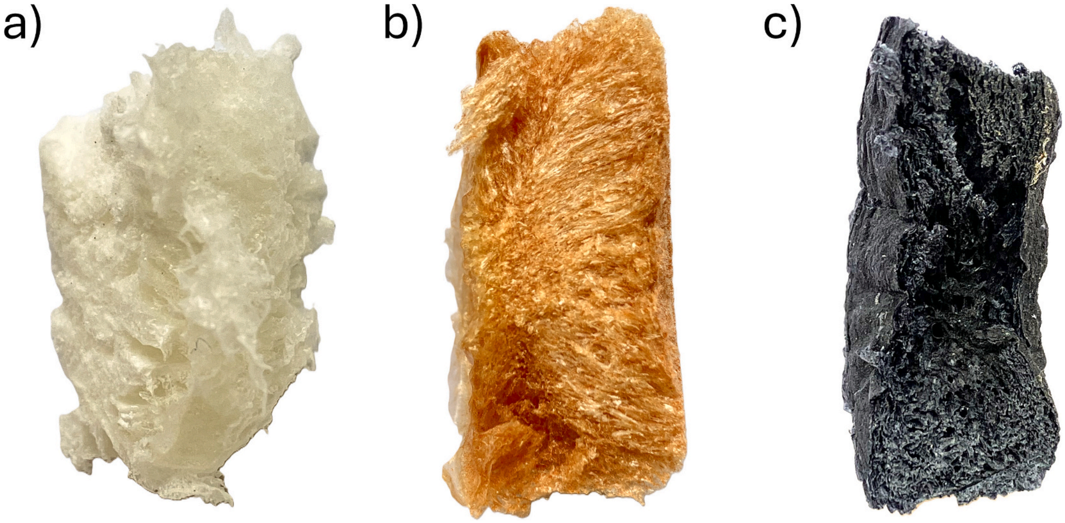

Fig. 2. Freeze-dried filled hydrogels a) without GTA or GN, b) with GTA, and c) with GN for XRD experiments. The characteristic yellowish reaction coloring (GTA) and the dark bluish reaction coloring (GN) are clearly visible.

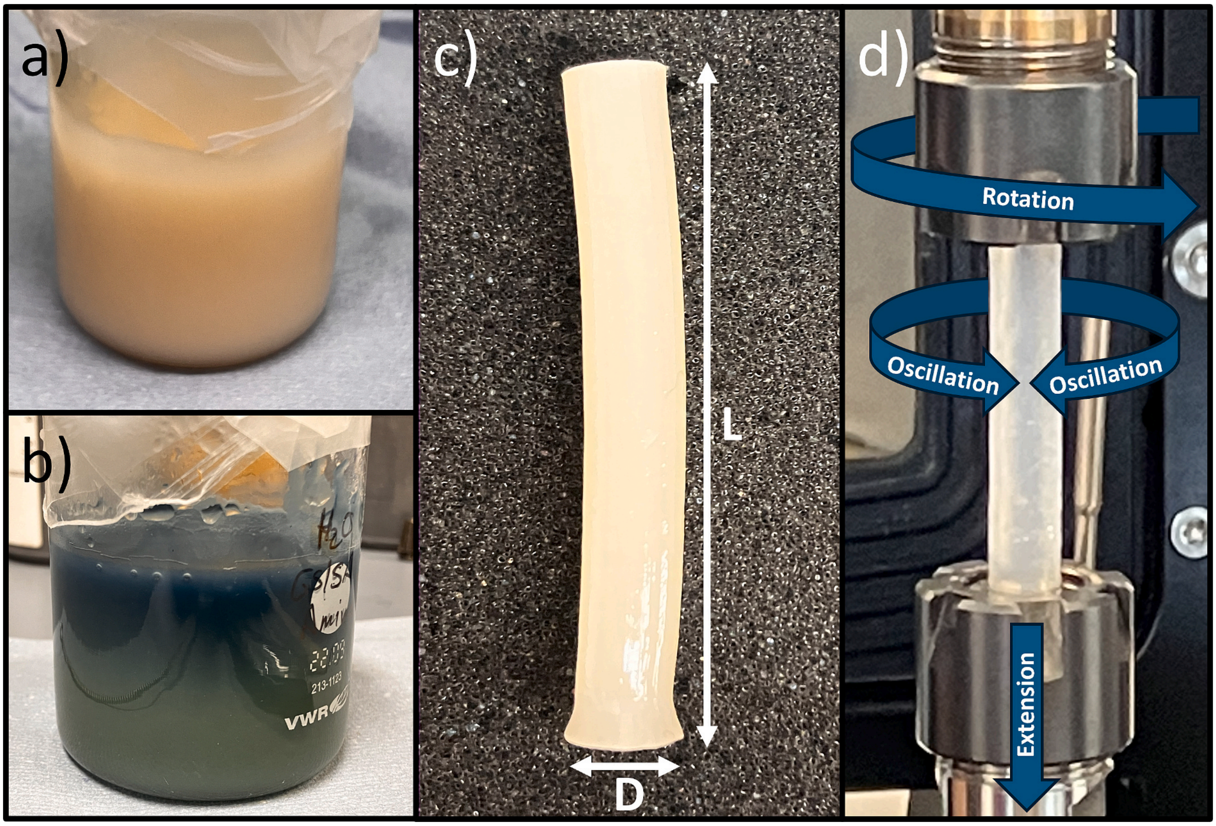

Fig. 3. Filled hydrogels with a) GTA and b) GN. c) A cylindrical sample cutout from the GTA hydrogel, where L and D indicate the length and diameter of the sample respectively. d) A clamped cylindrical sample in the DMA geometry. Arrows indicate the different types of dynamic deformations that can be applied.

of $\varphi = 1^\circ/\text{s}$. The sample was monitored and manually terminated when breakage or slippage occurred. Results are depicted in Fig. 10. Each curve corresponds to a single measurement with a fresh sample.

2.3. *Particle characterization: size and shape*

Particle sizing was first performed using the laser diffraction particle size analyzer Litesizer DIF 500 (Anton Paar). Additionally, particle size and shape were estimated using the dynamic image analyzer Litesizer DIA 700 (Anton Paar). In both instruments, particles were dispersed in a chamber containing water flowing toward the measuring cell. Fraunhofer model was used for diffraction data reconstruction. The results are shown in Fig. 4, in Fig. S1 in the Supplementary Material, and in Tables 1 and 2.

2.4. *FT-IR*

The experiments were performed using a Lyza 7000 Fourier-transform infrared (FT-IR) spectrometer (Anton Paar) with an internal reflection infrared spectroscopy (IRIS) single-reflection diamond attenuated total reflectance (ATR) accessory (PIKE Technologies). The resulting spectra in Fig. 7 correspond to the average of 24 scans. The error bars are negligible.

2.5. *XRD*

Experiments were carried out using a D8 Advance (Bruker), equipped with a position-sensitive detector (PSD) Lynxeye® using θ-θ geometry. A slit of variable divergence and a Soller slit of 2.3° were utilized. Data acquisition was performed in a 2θ range from 5° to 85° at 0.5 s per $0.013^\circ 2\theta$ step, resulting in a total count time of 96 s per step using the PSD. Anodes of Cu, with Cu Kα1,2 radiation ($\lambda = 0.154018$ nm), were used. The resulting data are shown in Fig. 6.

2.6. *SEM*

SEM images were recorded using a Quanta 400 ESEM (FEI, Germany). Freeze-dried samples were placed onto a carbon adhesive disk (no gold coating was applied). The samples were transferred to the SEM and evacuated directly to ESEM conditions (100 Pa chamber pressure, medium = water). Imaging was done using a Large Field Detector (LFD). Magnifications and acceleration voltages are shown in each micrograph (Fig. 5).

2.7. *Zeta potential*

The surface charge evolution of the functionalized silica was measured using a Litesizer DLS 701 (Anton Paar) equipped with a module FM 11. Smoluchowski approximation was used for calculation. The temperature was adjusted to 25 °C, and the measuring angle was 15°. The estimated Zeta potentials at each pH (5.14, 6.16, and 7.02) are an average of four measurements of the Zeta potential distributions.

2.8. *pH monitoring*

To quantify the reaction kinetics between the activators and the amino-functionalized silica, the pH of the particle-polymer dispersions was monitored in real-time using a pH electrode SY pH 325 (IKA) in combination with a measuring device ALMEMO 2490–2 (Ahlborn), at reaction temperatures (80 °C and 50 °C). This setup captured the acidification associated with the consumption of primary amines. However, as it was previously mentioned, direct monitoring during the gelation stage is unfeasible as the transition from a liquid to a solid matrix compromises sensor accuracy and probe maintenance. To circumvent

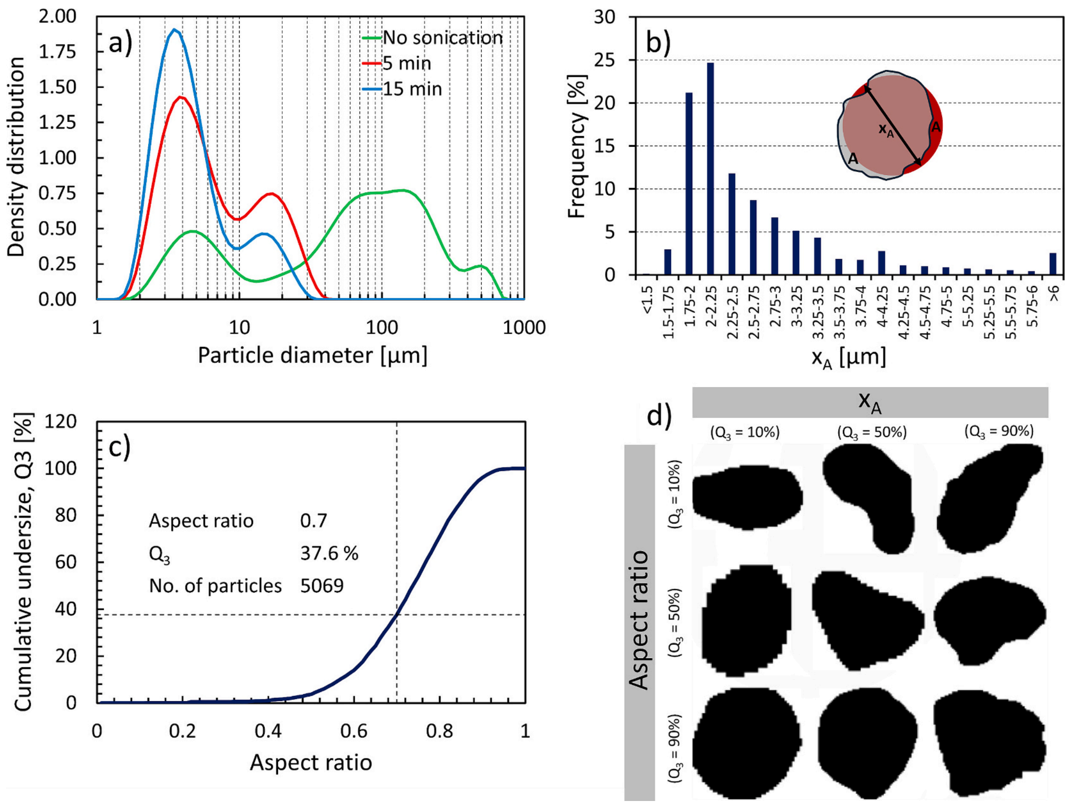

Fig. 4. a) Volume-weighted particle size distribution obtained from laser diffraction without (green line) and with ultrasonication at 30 W for 5 min (red line), and 15 min (blue line), b) number-weighted particle size histogram obtained from dynamic imaging, c) volume-weighted cumulative distribution of the particles aspect ratio determined by dynamic imaging, and d) particle shape obtained from dynamic imaging. (For interpretation of the references to color in this figure legend, the reader is referred to the web version of this article.)

Table 1
Volume-weighted particle sizes obtained from laser diffraction measurements. The D values (D_{10}, D_{50}, D_{90}) indicate the particle diameter that is undercut by 10%, 50% and 90% of the particles (e.g. D_{10} ➔ 10% of the particles have a smaller diameter than this value).

Duration of ultrasound at 30 W	D_{10} [µm]	D_{50} [µm]	D_{90} [µm]	Mean size [µm]	Span
0 s	4.19	65.83	240.11	101.86	3.58
5 min	2.59	5.26	19.03	8.32	3.13
15 min	2.33	3.97	13.32	5.82	2.77

Table 2
Particles sizes (x_A) obtained from dynamic image analysis measurements. The Q values (Q_{10}, Q_{50}, Q_{90}) indicate the particle diameter that is undercut by 10%, 50% and 90% of the particles (e.g. Q_{10} ➔ 10% of the particles have a smaller diameter than this value).

Weighting	Duration of ultrasound at 30 W	Q_{10} [µm]	Q_{50} [µm]	Q_{90} [µm]	Mean size [µm]	Span
Number	7 min	1.8	2.2	3.9	2.6	–
Volume	7 min	2.4	6.9	24.8	10.7	3.23

this, the process was simulated using standard acetic acid/sodium hydroxide buffer solutions calibrated to an initial pH matching that of the actual polymer precursors. For these simulated trials, the pH was monitored continuously under identical temperature conditions until a constant value was reached, ensuring a precise and complete measurement of the chemical environment while maintaining the liquid state required for reliable sensor electrode performance.

3. Results and discussion

3.1. Particle characterization

The particle size distributions and particle shapes are presented in Fig. 4. The particles were investigated in liquid dispersion in water. For the laser diffraction experiments (Fig. 4a), the particles were measured before (green line) and after ultrasonication at 30 W for 5 min (red line), and 15 min (blue line). The particle size distributions showed clearly how the agglomerates were dispersed into primary particles by ultrasound (Fig. 4a and Table 1). The number-weighted particle size distribution obtained from dynamic image analysis (Fig. 4b) revealed that most of these primary particles had a diameter of 2–3 µm. Here, the particle diameter, or the equivalent area diameter x_A, corresponds to the diameter of a circle with the same area as that of the detected particle. The equivalent area diameter can be defined as $x_A = \sqrt{4A/\pi}$, where A is the area of the cross-section of the detected particle. The volume-weighted size distribution obtained from dynamic image analysis coincides with the distribution obtained from laser diffraction after ultrasonication (see Table 2 and Fig. S1 in Supplementary Material). These results align with the supplier description and present a size distribution with a degree of polydispersity. The polydispersity was estimated using the span parameter, which measures the distribution width and is defined as $\left(D_{v,90} - D_{v,10}\right)/D_{v,50}$ (see Table 1; analog calculation of the span from the Q values in Table 2). The span was reduced by ultrasonication, however, after 15 min it was still 2.7, suggesting that the size distribution was still broad, i.e., polydisperse [37]. The particles shape can be characterized via the aspect ratio which was studied using dynamic image analysis (Fig. 4c). The aspect ratio ranges from 0 to 1, where 1 corresponds to the aspect ratio of a perfect sphere. The majority of particles (~ 62%) had an aspect ratio > 0.7, and therefore, could be

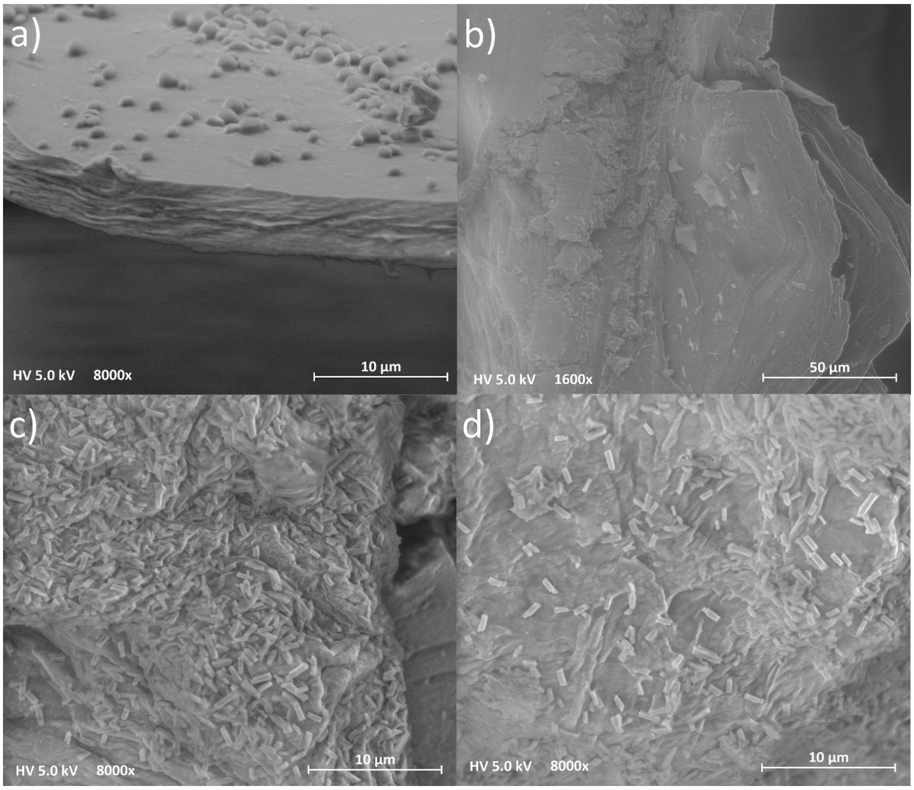

Fig. 5. SEM images of freeze-dried hydrogels containing silica particles for a) GG/SA hydrogel, b) GG_GTA/SA_GTA hydrogel, c) and d) GG_GN/SA_GN hydrogel. HV as 5.0 kV for all the experiments. Magnification of 8000× is shown for a), c) and d). Magnification of 1600× is shown for b). Scale bar for a), c), and d) corresponds to 10 μm. Scale bar for b) corresponds to 50 μm.

considered to be quasi-spherical. Fig. 4d shows representative particles of different sizes and aspect ratios.

3.2. *Reaction kinetics and surface charge evolution*

The reinforcement mechanism was elucidated through quantitative in-line pH kinetics and surface charge evolution analysis. To move beyond qualitative observations of color changes, the reaction kinetics between the amino-functionalized silica particles and the bifunctional activators (GTA and GN) were quantified via in-line pH monitoring. As shown in Fig. S3, the addition of amino-functionalized silica to the initial GG/SA solution (pH ≈ 5.4) caused an immediate shift to an alkaline environment (pH ≈ 8.8). Subsequent addition of the activators induced acidification. GN exhibited a slower, more controlled pH decrease compared to the rapid drop observed with GTA. The chemical environment during the gelation stage was further validated using model acetic acid/sodium hydroxide solutions, which captured the pH drop upon the addition of GDL and $CaCO_3$ (Fig. S4). This pH evolution directly governs the electrostatic landscape at the particle-polymer interface. Zeta potential distributions (Fig. S2) revealed the surface charge transitions at critical pH values encountered during the reaction. These values are summarized in Table 3.

The synchronization of pH-dependent surface charge with the onset of gelation is the primary driver for the observed reinforcement. As shown in Fig. S3, the onset of gelation, triggered by the addition of GDL and $CaCO_3$, occurs at different pH baselines depending on the surface activator used. For the control polymer solution (without GTA or GN), gelation begins at a highly alkaline pH of approximately 9.0. In the GG/SA hydrogel with GTA, the baseline pH at the onset is approximately 8.0. However, for the hydrogel with GN, the baseline pH at the moment of crosslinker addition is significantly lower, at approximately 6.3. This distinction is critical when viewed alongside the Zeta potential data in Table 3. Among the three scenarios, the hydrogel with GN is the only one that shifted the environment into the “electrostatic window” (pH 6–7) prior to gelation. In this range, the silica particles exhibited their minimum negative charge magnitude (−11.5 ± 1.5 mV). Although both the silica particles and the polymer chains remained negatively charged, the GN-induced acidification effectively reduced the electrostatic repulsive barrier between them more than in the other hydrogels. By bringing the surface charge closer to the point of zero charge during the critical period of network formation, GN facilitated a higher degree of interfacial proximity. This reduction in repulsion allowed for the transition from simple physical entrapment to the likely covalent anchoring. Consequently, part of the superior mechanical performance of the GN-activated hydrogels was attributed to the ability to prime the electrostatic landscape, ensuring that the particles were effectively integrated rather than repelled during the gelation process.

Table 3
Zeta potential of amino-functionalized silica particles at critical pH points.

pH	5.14	6.16	7.02
Zeta potential [mV]	20.9 ± 0.9	−11.5 ± 1.5	−15.3 ± 1.19

3.3. *Interfacial morphology (SEM)*

The interfacial characteristics of the freeze-dried hydrogels were examined via SEM to evaluate the distribution and integration of the amino-functionalized silica particles within the polymer matrix (Fig. 5). In the GG/SA hydrogel (Fig. 5a), the polymer matrix exhibited a layered morphology, likely resulting from the sublimation of ice crystals during the freeze-drying process. The amino-functionalized silica particles appeared as discrete, spherical entities that were embedded within the polymer matrix walls. While the particles were clearly covered by a thin layer of the polymer, their quasi-spherical shape remained well-defined. This visual evidence suggests a mechanism dominated by physical entrapment [38,39]. In this framework, the particles appeared to be immobilized, with the polymer matrix acting as a physical cage rather than a covalent cage.

For the GG/SA hydrogel with GTA (Fig. 5b), a morphological shift is observed. The layered structure seen in the GG/SA hydrogel is replaced by a different texture that suggests a higher degree of structural disorganization. Interestingly, the amino-functionalized silica particles were no longer visible at the surface. This could be interpreted as an integration state where the rapid reaction kinetics of GTA potentially promoted a high-efficiency but disorganized encapsulation of the particles. It is hypothesized that the bifunctional nature of GTA facilitates an immediate cross-linking that buries or "mask" the particles deep within the polymer matrix. This effect, combined with the lack of a defined porous network, was assumed to reflect a more fragile or less structurally optimized interfacial state compared to the hydrogel with GN.

In contrast, the hydrogel with GN (Fig. 5c and d) exhibited a significantly more complex and textured morphology. The polymer surface showed a distinctly increased roughness compared to the relatively smooth walls of the GG/SA hydrogel without GTA or GN. This texture could be a consequence of the localized GN-mediated cross-linking, which could alter the assembly of the polymer chains during gelation. Furthermore, it is also observed the formation of rod-like structures localized specifically at the particle–polymer boundaries. These elongated, anisotropic protrusions could indicate a transition to a polymer-directed assembly or seeded growth mechanism [40], where the silica particles would be the seeds. It is hypothesized that the "electrostatic window" at pH 6.3 allowed for a slower, more organized assembly of GN-polymer complexes. This ordered growth might facilitate a more effective interfacial interlocking, related to both surface roughness and rods. These features could be the physical manifestation of a deeper structural transformation, likely correlated with the significant shift observed in the XRD diffraction patterns.

3.4. XRD

The X-ray diffraction (XRD) diffractograms (Fig. 6) were used to characterize the crystalline structures of the lyophilized hydrogels (both unfilled and filled) and the pure $CaCO_3$ powder. All patterns exhibited sharp, characteristic diffraction peaks for $CaCO_3$ in the 2θ range 29.4° to 65.7°, with the most prominent reflection appearing at approximately 29.4° [26,41]. This finding confirms the highly crystalline nature of the incorporated $CaCO_3$. For the polymer matrix components, the GG and GG/SA samples showed broad peaks spanning from 5.5° to 21.5°, consistent with the semi-crystalline structure reported for GG [42]. Significantly, the patterns indicate that no novel crystalline phases were generated.

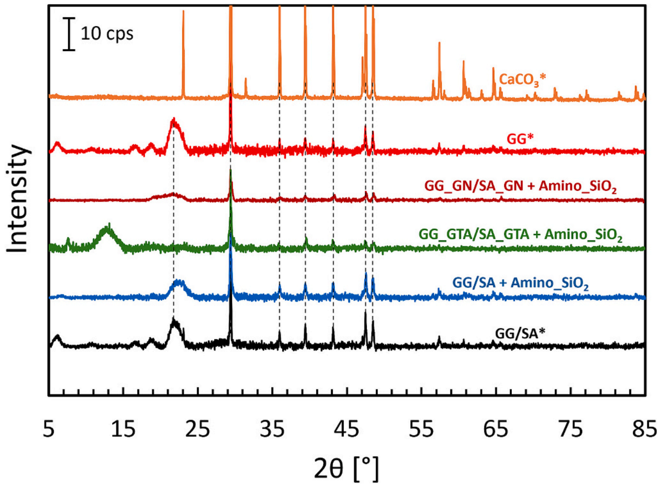

Fig. 6. XRD patterns, with background subtracted, for the unfilled and filled lyophilized hydrogels and pure $CaCO_3$ powder. Dashed lines highlight the alignment of corresponding characteristic peaks across the different diffractograms. The vertical scale bar represents 10 counts per second (cps). Data marked with * corresponds to results from our previous study [26].

The filled GG/SA hydrogel exhibited a broader peak centered at approximately 23°, which is a characteristic feature of amorphous silica (SiO_2) and supports the findings from our previous work [26]. Interestingly, the presence of amine-functionalized particles suppressed smaller peaks located at angles below 23°, which were present in the unfilled hydrogel diffraction pattern. This could indicate a subtle transition toward more disordered arrangements as the particles are physically embedded within the layered polymer walls observed in SEM.

Notably, the addition of GTA or GN introduced significant modifications in the XRD patterns. In the case of GTA, the peak at 23° disappeared, and a new, broader peak emerged at around 13°. The disappearance of the characteristic peak for amorphous silica at 23° could be related to the existence of covalent bonding between the amino groups on the surface of the particles and GTA. In a fundamentally equivalent case, the gelation of chitosan and GTA resulted in a substantial decrease of the crystalline peak associated with pure chitosan at 20° [43]. These observations indicate a rapid and aggressive reaction, which is common for GTA, as mentioned before. The appearance of the peak at lower angles is likely related to a new structural order where GTA and silica particles increase the interchain spacing, potentially signifying a new hybrid phase at the interface between the particles and the surrounding polymer matrix. This suggests that despite the fragile appearance seen in SEM, a substantive chemical integration has occurred, albeit in a potentially disordered manner.

On the other hand, the addition of GN substantially reduced the intensity of the peak and broadened it. These changes can be attributed to the GN-silica reaction, which leads to more amorphous states and an increase in structural tension [44]. In contrast to GTA, no new peaks were observed with GN, indicating the slower and milder reaction nature of GN. It is hypothesized that the distinct surface roughness and rod-like structures observed in SEM were the morphological manifestations of this increased tension and the more controlled assembly of GN-polymer complexes. This suggests that GN facilitates a more localized and organized interfacial interlocking compared to the rapid phase transition seen with GTA, providing the structural basis for the mechanical reinforcement observed in the hybrid network.

3.5. FT-IR

Results from FT-IR experiments are presented in Fig. 7. Main peaks corresponding to the common vibrational modes of GG and SA molecules appeared for all hydrogels at 1030 cm^{-1}, 1400 cm^{-1}, 1600 cm^{-1}, and 2911 cm^{-1} corresponding to C—O, symmetric carboxyl group, asymmetric carboxyl group, and C—H bonds, respectively. Additionally, the common stretching band for O—H appeared for all spectra between 3137 cm^{-1} and 3460 cm^{-1}. This suggests there was no significant interaction between GG and SA networks. Interestingly, the presence of silica particles was only identified due to the appearance of a fifth peak in the interval 400–500 cm^{-1}, which was absent in unfilled hydrogels. These peaks correspond to δ Si—O, an internal O-Si-O bending [45,46], and are indicated by arrows in Fig. 7. The addition of GTA or GN did not introduce new peaks, as could be expected for C═N bonds, which typically appear between 1640 and 1690 cm^{-1} [47]. However, as evidenced by the change in color during the reaction and the increases in storage moduli, the formation of covalent linkages is plausible. Notably, the FT-IR results suggest that the number of covalent links formed is too low to be detected but enough to enhance mechanical improvements. This limited detection threshold is consistent with the masking and interfacial phenomena discussed in the previous sections. In the case of the hydrogel with GTA, the absence of clear C═N bonds despite the aggressive reaction suggested by XRD and the fragile morphology in SEM further supports the assumption that the covalent integration is

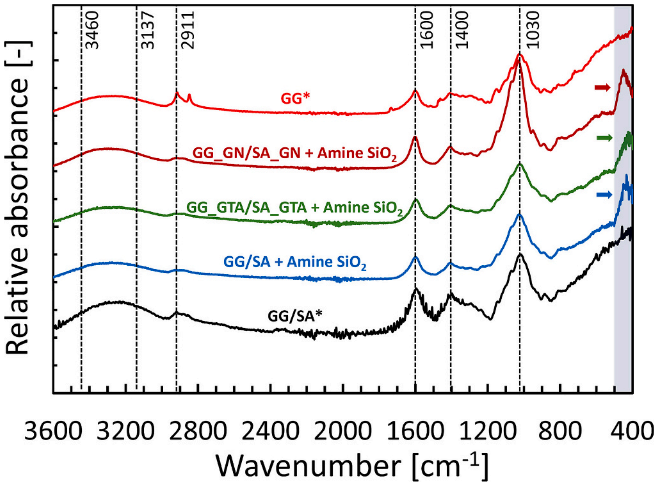

Fig. 7. Relative absorbances for FT-IR experiments on the filled and unfilled dried hydrogels are presented. Prominent pattern peaks are identified by their corresponding wavenumbers and highlighted using vertical dashed black lines. The shaded area represents the interval of 400–500 cm^{-1}, where peaks corresponding to silica are observed. Colored arrows indicate the peak for each spectrum. Each pattern was normalized by its highest value and displaced along the Y-axis. Data marked with * corresponds to results from our previous study [26].

confined to a dense, localized hybrid phase at the particle surface. Conversely, for the hydrogel with GN, while the molecular bridging remains below the FT-IR detection limit, the distinct surface roughness and rods observed in SEM, coupled with the structural tension indicated by peak broadening in the XRD pattern, provide the physical evidence for these subtle chemical changes. The overlapping of the Si-O-Si asymmetric stretching band with the C—O band at 1030 cm^{-1} may further obscure the specific interfacial signatures of the silica-polymer bond, yet the totality of the evidence strongly points toward a successful, albeit spatially restricted, covalent bridging. The corresponding stretching bands are shown in Table 4.

Table 4
Stretching band assignments for FT-IR spectra peaks shown in Fig. 7.

Wavenumber [cm^{-1}]	Material	Stretching band	Reference
400–500 (shaded area)	Silica	δ Si-O: Internal O-Si-O bending	Ellerbrock et al. [45]; Ulfa et al. [46]
1030	Alginate & Gellan; silica	C-O; asymmetric stretching Si-O-Si (band overlapping)	Modrogan et al. (2020) [48]; Sarker et al. (2014) [49]; Panday et al. (2023) [50]; Wang et al. (2021) [51]
1400	Alginate & Gellan	Symmetric carboxyl group	Modrogan et al. (2020) [48]; Sarker et al. (2014) [49]; Panday et al. (2023) [50]; Wang et al. (2021) [51]
1600	Alginate & Gellan	Asymmetric carboxyl group	Modrogan et al. (2020) [48]; Sarker et al. (2014) [49]; Panday et al. (2023) [50] Wang et al. (2021) [51]
2911	Alginate & Gellan	C-H	Panday et al. (2023) [50]
3137–3460	Alginate & Gellan	O-H	Modrogan et al. (2020) [48]; Panday et al. (2023) [50]

3.6. *Amplitude sweeps*

Results for strain amplitude sweeps are depicted in Fig. 8, where the torsional and extensional storage moduli are shown as functions of shear strain and extensional strain respectively. The loss moduli are not presented in the graphs because relevant information was absent.

In both torsional (Fig. 8a) and extensional (Fig. 8b) deformations, the pure GG hydrogel exhibited the highest storage moduli, related to the longer polymer chains of GG. This finding aligns with results for the GG/SA hydrogel, which showed the lowest storage moduli. The presence of SA weakens the microstructure due to its shorter polymer chains. However, the pure GG hydrogel has both LVRs in torsion and extension restricted to smaller strain amplitudes. The interpenetrating network created between the two polymers provides two main benefits: the GG network provides stiffness, determining the magnitude of the storage moduli, while the SA network offers softness and ductility, reflected in an extended LVR. For isotropic materials, as is the case here, the absolute complex Young's modulus, $|E^*| = \sqrt{(E')^2 + (E'')^2} \approx |E'|$, is 2–3 times higher than the absolute complex shear modulus $|G^*| = \sqrt{(G')^2 + (G'')^2} \approx |G'|$ [35], where G'' and E'' are neglected compared with their elastic counterparts. The mechanical behavior of the hydrogels can also be described in terms of the absolute complex Poisson's ratio, $|\nu^*|$, defined as

$$|\nu^*| = \sqrt{\frac{|E^*|^2}{4|G^*|^2} - \frac{|E^*|}{|G^*|}cos(\delta_E - \delta_G) + 1} \tag{1}$$

where δ_G and δ_E are the phase shift angles for torsional and extensional measurements, respectively [35]. For the pure GG hydrogel, Poisson's ratio estimated in the LVR was 0.32 ± 0.03, which is below the Poisson's ratio of 0.44 ± 0.06 obtained for the GG/SA hydrogel [26]. Higher values of the absolute complex Poisson's ratio, closer to the maximum of 0.5, are associated with more compliant, ductile, and soft materials, as is the case with the GG/SA hydrogel. Lower values of the absolute complex Poisson's ratio, as observed for the pure GG hydrogel, reflect a less compliant, stiff, and brittle nature.

When particles were added without GTA or GN, increases in the storage moduli of 10% in torsion, and 15% in extension were observed compared with the unfilled hydrogel. This enhancement in storage moduli for the filled systems could be a direct macroscopic consequence of the interfacial reinforcements observed in SEM. Specifically, the modest increase in stiffness is likely related to the simple physical entrapment of the amino-functionalized particles within the multilayer polymer walls. Notably, the increase in the extensional storage modulus was proportionately higher than that in torsion. This difference may be related to the particles acting as stress concentrators and load-bearing elements [52,53]. In extension, polymer chains tend to align along the stretching direction and occasionally align around the particles. Here, the particles act as bridges through which tensile stress could be transferred. This leads to a more pronounced increase in the extensional storage modulus compared with its torsional counterpart, where the polymer matrix circumvents the particles more easily, thereby reducing their contribution to mechanical improvement. The estimated absolute complex Poisson's ratio has an average value of 0.48 ± 0.02 in the LVR, which is slightly higher than the corresponding value for the unfilled GG/SA hydrogel. The presence of fillers enhances the mechanical properties of the hydrogel while simultaneously introducing a more ductile (higher Poisson's ratio) character to the hydrogel. This is evidenced by the results in Fig. 8, where the LVRs for torsion and extension were clearly extended, especially in extension. The significant extension of the LVR in these filled systems likely reflects a more robust, particle-bridged network that can accommodate larger deformations before structural breakdown. This expansion could be explained by the polydispersity of the particle sizes: as the mechanical failure of different

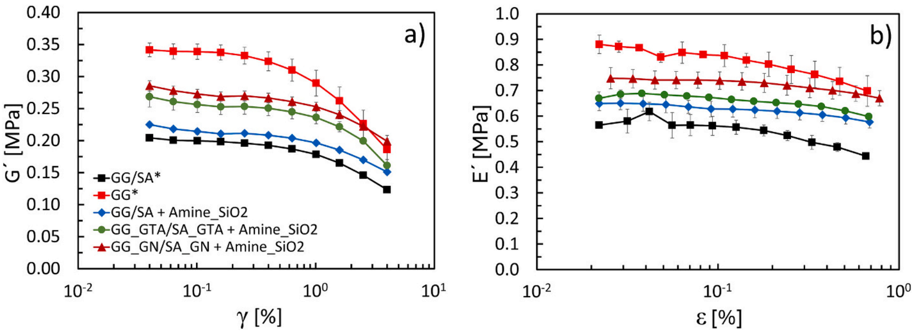

Fig. 8. Strain amplitude sweep tests in a) torsion and b) extension for the unfilled and filled hydrogels. Torsional storage modulus (*G*') and extensional storage modulus (*E*') are shown as functions of shear strain (γ) and extensional strain (ε), respectively, for *T* = 30 °C and *RH* = 90%. Data marked with * corresponds to results from our previous study [26]. These results highlight the strengthening of the elastic properties as a function the hydrogel composition.

particle bridges depends on the available surface area, this leads to gradual yielding and a broader transition into the non-linear viscoelastic region [54].

The addition of GTA or GN to the filled hydrogels contributed to further increases in both torsional and extensional storage moduli (Fig. 8). GTA and GN molecules interact with the amino groups on the particle surface, forming covalent bonds. GTA reacts via Schiff base formation, forming C═N bonds [55], while GN triggers ring opening and subsequent ester linkage [44,47]. The increments in storage moduli for the hydrogel with GN were observed to be larger than those for the hydrogel with GTA. This difference appears to be less a result of simple particle-particle bridging and more a manifestation of the distinct morphologies and crystallographic states previously discussed. It is hypothesized that the fragile appearance of the GTA matrix in SEM reflects a poorly integrated state, where rapid covalent masking, associated with the specific XRD peak shift to 13°, prevents the formation of an organized interface between the particles and the polymer matrix. This aggressive reaction likely results in a dense, brittle shell that fails to effectively distribute stress into the bulk network. Conversely, the slower reaction kinetics of GN allows for the formation of the rod-like structures and surface roughness seen in SEM, which could facilitate superior mechanical interlocking. This rod-like growth provides a higher effective surface area for interaction, creating a more cohesive hybrid network. This is macroscopically evidenced by the hydrogel with GN exhibiting the most stable storage moduli and a highly resilient LVR. In terms of the absolute complex Poisson's ratio, both hydrogels with GTA and GN exhibited very similar average values of 0.32 ± 0.04 and 0.34 ± 0.02, respectively. These values indicate a return to a less compliant, stiff, and brittle nature similar to pure GG, yet the LVRs remained expanded compared with the unfilled hydrogel. This signifies that the interfacial chemistry, whether through aggressive particle masking or organized growth, successfully creates a hybrid network capable of delaying the onset of non-linear behavior by successfully transferring load through the covalent-organic interface.

3.7. Frequency sweeps

The experimental results are presented in Fig. 9. The values observed for both torsional and extensional storage moduli follow similar trends to those observed in the strain amplitude sweeps. The presence of particles alone introduced mechanical enhancement, and further improvements were observed when either GTA or GN were added, as explained in the case of strain amplitude sweeps. Despite the presence of particles and GTA or GN, the hydrogels exhibited the conventional behavior observed for interpenetrating polymer networks [56], where viscoelastic properties demonstrate minor dependency on angular frequency and follow nearly ideal power-law trends. The Poisson's ratios estimated at $\omega = 1$ rad/s align with those obtained from amplitude sweeps in the LVR, confirming consistency between the two experiments.

3.8. Breaking rod tests

Breaking rod test results for all hydrogels are shown in Fig. 10. The pure SA hydrogel was excluded from these experiments due to difficulties concerning reproducibility and stability due to extreme softness. Differences were observed at strains where the shear stresses reached a maximum. For unfilled and filled GG/SA gels without GTA or GN (Fig. 10a and c, respectively), average maximum shear stresses were found around 12 kPa, with corresponding shear strain $\gamma \sim$ 19–20%. In the case of the pure GG gel, the maximum shear stress was between 14 kPa and 17 kPa, with an average strain $\gamma \sim$ 15–16% (Fig. 10b). In the case of the filled GG/SA gel with GTA (Fig. 10d), the maximum shear stress oscillated between 12 kPa and 15 kPa, with an average strain of 24–26% at this point. Finally, for the filled GG/SA gel with GN (Fig. 10e), higher maxima for shear stress were observed, ranging from

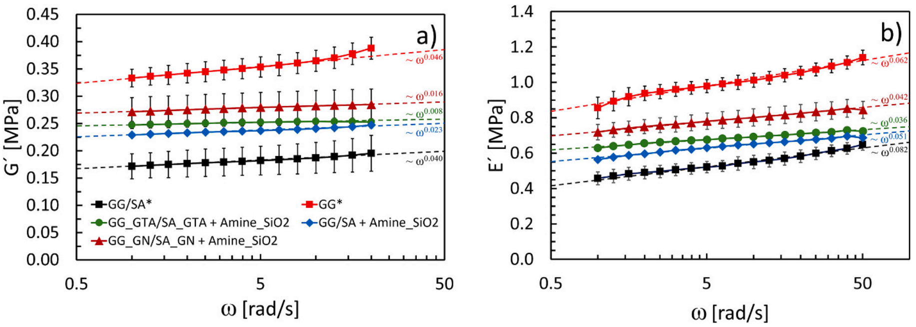

Fig. 9. Angular frequency sweeps in a) torsion and b) extension for the unfilled and filled hydrogels. Torsional storage modulus (*G*') and extensional storage modulus (*E*') are presented as functions of the angular frequency sweep (ω) for *T* = 30 °C and *RH* = 90%. Data marked with * corresponds to results obtained in our previous study [26]. Dashed lines indicate a power-law fitting. All coefficients of determination R^2 are larger than 0.85.

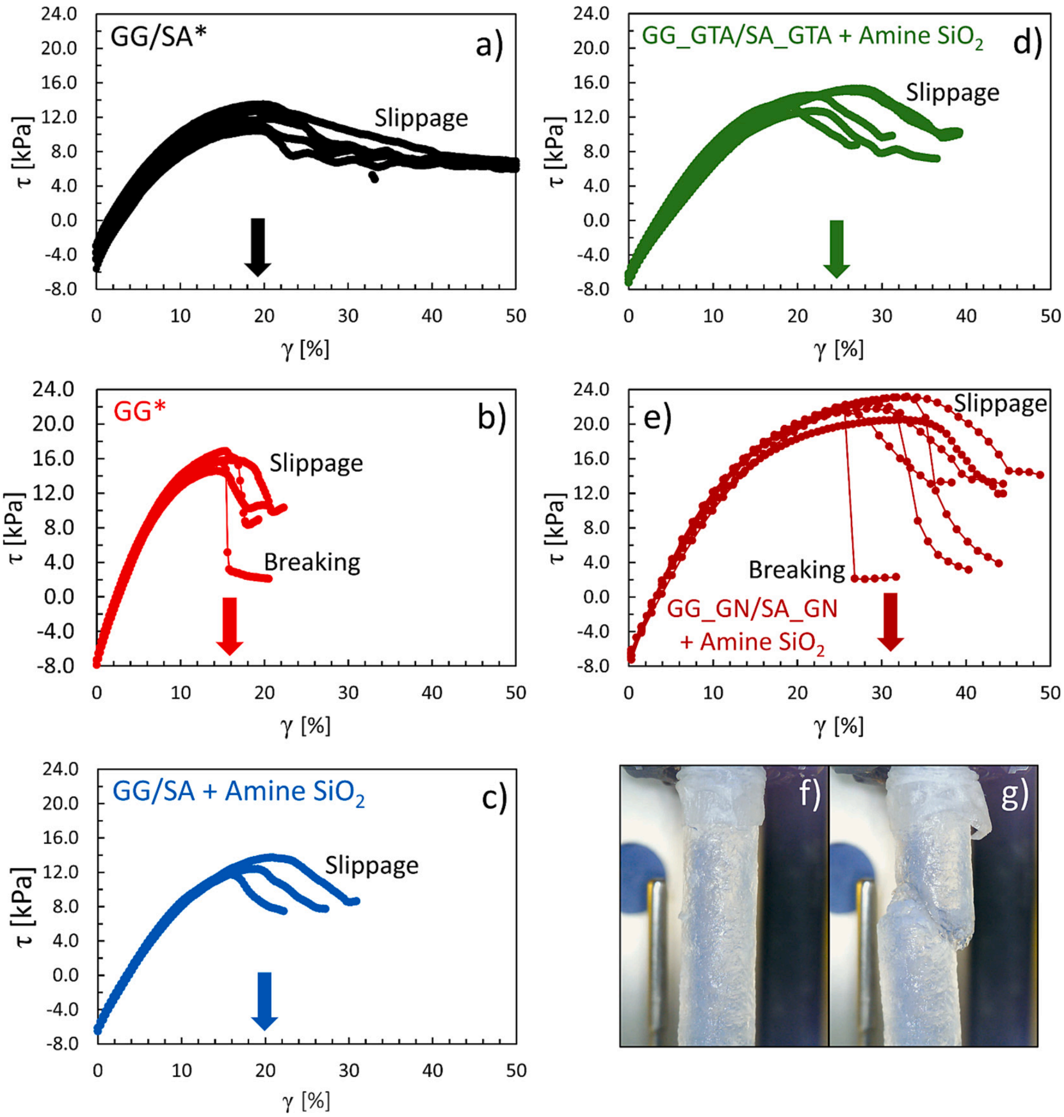

Fig. 10. Breaking rod tests in torsion for a) GG/SA, b) GG, c) filled GG/SA without GTA or GN, d) filled GG/SA with GTA, e) filled GG/SA with GN. Pictures of a cylindrical sample of GG f) before and g) after the breaking point are also shown. Data marked with * corresponds to results obtained in our previous study [26]. The results highlight the dependence of the strain at break on the different hydrogel compositions.

20 kPa to 24 kPa, with an average strain of 30–32% at this point.

Upon reaching the maximum shear stress, the hydrogels experienced breaking or slippage. Slippage can be a direct consequence of the water expelled through the cylinder surface due to applied deformation [57,58]. Excess water wets the hydrogel surface at the clamp positions, reducing friction and consequently inducing slippage. In our previous work [26], we performed breaking rod tests, which, as described there, showed slippage due to sweating or breaking. The breaking tests indicated that breaking was often observed for pure GG hydrogels, with the maximum stress reached at lower strains. The polymeric structure of pure GG hydrogels appeared harder but more brittle, withstanding smaller deformations.

The addition of particles without GTA or GN (Fig. 10c) did not significantly change the response in this test compared with the unfilled hydrogel. As previously noted, the maximum stress and strain were like those of the unfilled GG/SA gel (Fig. 10a). This minimal impact on ultimate strength aligns with the layered morphology observed in SEM, where particles are physically trapped within the polymer walls but lack a chemically integrated interface to reinforce the network against high-strain failure.

The use of GTA (Fig. 10d) introduced slight reinforcement by increasing the maximum stress, but more importantly by shifting the maximum strains to higher values, as indicated by the arrow. However, there was no significant increase in stress compared to the hydrogel without GTA or GN. This limited reinforcement is likely a consequence of the masking and fragile morphology discussed in previous sections. The aggressive reaction of GTA creates a rigid particle-particle network, but the rapid encapsulation of the silica surface hinders the formation of a cohesive, organized interface with the surrounding polymer matrix. This results in a localized hybrid phase that, while providing some ductility, lacks the structural integration required to significantly increase the stress at break.

The most significant changes were observed for the hydrogel with GN (Fig. 10e). The maximum stress was increased by a factor of around 1.8 with respect to the GG/SA hydrogels. Additionally, the maximum strain was again shifted to higher values (see arrow), and breaking events were again visible. Hence, the hydrogel with GN demonstrated the highest strain and stress at break, exhibiting excellent toughness. This superior performance is directly linked to the formation of the rod-like structures and increased surface roughness identified in SEM. These features facilitate a robust mechanical interlocking between the silica and the GG-SA network. Furthermore, the structural tension indicated by the amorphous broadening in XRD suggests that the hydrogel with GN creates a more resilient, highly integrated hybrid network. Unlike the brittle masking seen with GTA, the slower kinetics of GN allow for a more spatially distributed and organized covalent bridging, enabling the hydrogel to effectively dissipate energy and withstand significantly higher loads before failure.

4. Conclusion

This study examined the role of amine-functionalized mesoporous silica particles as active structural modifiers within GG/SA-based soft polymer networks, and the effect of the surface activation agents GTA and GN. We demonstrated that the mechanical reinforcement of these systems is governed by a dual-mechanism of interfacial structural assembly and covalent bridging.

Strain amplitude sweeps showed that the mere presence of particles without surface activation increases both torsional and extensional storage moduli. This enhancement is attributed to the physical entrapment of particles within the polymer walls, as identified in SEM. Furthermore, the particles induced a significant expansion of the linear viscoelastic regions (LVR), which can be attributed to the creation of a robust, particle-bridged network. The polydispersity of the particle sizes leads to gradual yielding, thereby broadening the transition into the non-linear viscoelastic region.

The addition of GTA or GN further increased the storage moduli and ultimate strength. The results indicate that the macroscopic mechanical response is strongly dictated by the reaction kinetics at the particle interface. In the case of GTA, the faster reaction kinetics lead to "masking", where a dense, localized hybrid phase encapsulates the silica particles. While this provides a rigid particle-particle network, the XRD shift to 13° and the fragile morphology observed in SEM suggest a disorganized interface that limits energy dissipation, resulting in a more brittle reinforcement. In contrast, the slower reaction kinetics of GN facilitates the growth of rod-like structures and increased surface roughness. This morphology, coupled with the structural tension indicated by XRD amorphous broadening, promotes superior mechanical interlocking between the particles and polymer matrix. Consequently, the hydrogel with GN demonstrated the highest response in breaking rod tests, exhibiting excellent toughness and a significantly higher stress at break compared to the GTA system. Remarkably, we found that FT-IR could not detect the C═N bonds associated with the covalent linkages, suggesting that the number of covalent bonds, while sufficient to modify macroscopic properties, remains below the infrared detection threshold or is obscured by band overlapping. In summary, this work demonstrates that the mechanical properties of a model biocompatible hydrogel can be tailored by controlling the interfacial assembly. By utilizing GN as a natural, slower-reacting substitute for GTA, it is possible to transition from simple particle "masking" to a highly integrated, hybrid network, offering a pathway toward the design of high-performance, drug-carrying scaffolds with optimized mechanical resilience.

CRediT authorship contribution statement

Juan Pablo Segovia-Gutiérrez: Writing – review & editing, Writing – original draft, Methodology, Formal analysis, Conceptualization. **José Alberto Rodríguez Agudo:** Writing – review & editing, Writing – original draft, Investigation, Conceptualization. **Sönke Wengler-Rust:** Writing – review & editing, Investigation, Formal analysis. **Nicolas Binder:** Writing – review & editing, Investigation, Formal analysis. **Peter Georg Weidler:** Writing – review & editing, Writing – original draft, Investigation, Formal analysis, Conceptualization. **Frank Kirschhöfer:** Writing – review & editing, Writing – original draft, Investigation, Formal analysis, Conceptualization. **Jürgen Utz:** Writing – review & editing, Resources, Project administration. **Natalie Germann:** Writing – review & editing, Supervision, Resources, Project administration, Methodology, Formal analysis, Conceptualization.

Declaration of competing interest

The authors declare that they have no known competing financial interests or personal relationships that could have appeared to influence the work reported in this paper.

Acknowledgments

We acknowledge support from the Deutsche Forschungsgemeinschaft (DFG) for the research equipment used in this study (Project No. 544360563). The authors would like to thank Prof. Dr. Lola González-García (INM – Leibniz Institute for New Materials) for providing access to the electron microscopy facilities. Special thanks are extended to Dominik Perius for his invaluable technical assistance and expertise in the acquisition of the SEM images presented in this work.

Appendix A. Supplementary data

Supplementary data to this article can be found online at https://doi.org/10.1016/j.jcis.2026.140912.

Data availability

Data will be made available on request.

References

[1] E.M. Ahmed, Hydrogel: preparation, characterization, and applications: a review, J. Adv. Res. 6 (2015) 105–121.
[2] N. Anjum, N. Joyal, J. Iroegbu, D. Li, C. Shen, Humidity-modulated properties of hydrogel polymer electrolytes for flexible supercapacitors, J. Power Sources 499 (2021) 229962.
[3] T. Dutta, P. Chaturvedi, I. Llamas-Garro, J.S. Velázquez-González, R. Dubey, S. K. Mishra, Smart materials for flexible electronics and devices: hydrogel, RSC Adv. 14 (2024) 12984.
[4] E. Caló, V.V. Khutoryanskiy, Biomedical applications of hydrogels: a review of patents and commercial products, Eur. Polym. J. 65 (2015) 252–267.
[5] M. Jridi, S. Bardaa, D. Moalla, T. Rebaii, N. Souissi, Z. Sahnoun, M. Nasri, Microstructure, rheological and wound healing properties of collagen-based gel from cuttlefish skin, Int. J. Biol. Macromol. 77 (2015) 369–374.
[6] R. Subramani, A. Izquierdo-Alvarez, P. Bhattacharya, M. Meerts, P. Moldenaers, H. Ramon, H. Van Oosterwyck, The influence of swelling on elastic properties of polyacrylamide hydrogels, Front. Mater. 7 (2020) 212.
[7] S. Wang, J. Liu, L. Wang, H. Cai, Q. Wang, W. Wang, J. Shao, X. Dong, Underwater adhesion and anti-swelling hydrogels, Adv. Mater. Technol. 8 (2023) 2201477.
[8] Q. Li, B. Tian, G. Tang, H. Zhan, J. Liang, P. Guo, Q. Liu, W. Wu, Multifunctional conductive hydrogels for wearable sensors and supercapacitors, J. Mater. Chem. A 12 (2024) 3589–3600.
[9] S. Chervinskii, I. Issah, M. Lahikainen, A.R. Rashed, K. Kuntze, A. Priimagi, H. Caglayan, Humidity- and temperature-tunable metal–hydrogel–metal reflective filters, Appl. Mater. Interfaces 13 (2021) 50564–50572.
[10] X. Hu, S. Qu, Inclusion size effect on mechanical properties of particle hydrogel composite, Acta Mech. Solida Sin. 32 (2019) 643–651.
[11] D.K. Makepeace, P. Locatelli, C. Lindsay, J.M. Adams, J.L. Keddie, Colloidal polymer composites: are nano-fillers always better for improving mechanical properties? J. Colloid Interface Sci. 523 (2018) 45–55.
[12] S.R. Van Tomme, C.F. van Nostrum, M. Dijkstra, S.C. De Smedt, W.E. Hennink, Effect of particle size and charge on the network properties of microsphere-based hydrogels, Eur. J. Pharm. Biopharm. 70 (2008) 522–530.
[13] M. Laurati, G. Petekidis, N. Koumakis, F. Cardinaux, A.B. Schofield, J.M. Brader, M. Fuchs, S.U. Egelhaaf, Structure, dynamics, and rheology of colloid-polymer mixtures: from liquids to gels, J. Chem. Phys. 130 (2009) 134907.
[14] K. Suresh, G. Kumaraswamy, Effect of electrostatic interactions on structure and mechanical properties of ice templated colloid-polymer composites, J. Phys. D. Appl. Phys. 52 (2019) 214002.
[15] A.V. Karatrantos, C. Mugemana, L. Bouhala, N. Clarke, M. Kröger, From ionic nanoparticle organic hybrids to ionic nanocomposites: structure, dynamics, and properties: a review, Nanomaterials 13 (1) (2023) 2.
[16] G. Rezvan, M. Esmaeili, M. Sadati, N. Taheri-Qazvini, Hybrid colloidal gels with tunable elasticity formed by charge-driven assembly between spherical soft nanoparticles and discotic nanosilicates, J. Colloid Interface Sci. 627 (2022) 40–52.
[17] M. Bailly, M. Kontopoulou, K. El Mabrouk, Effect of polymer/filler interactions on the structure and rheological properties of ethylene-octene copolymer/nanosilica composites, Polymer 51 (2010) 5506–5515.
[18] C.G. França, T. Plaza, N. Naveas, M.H.A. Santana, M. Manso-Silván, G. Recio, J. Hernandez-Montelongo, Nanoporous silicon microparticles embedded into oxidized hyaluronic acid/adipic acid dihydrazide hydrogel for enhanced controlled drug delivery, Microporous Mesoporous Mater. 310 (2021) 110634.

[19] D. Hense, O.I. Strube, Glutaraldehyde cross-linking of salt-induced fibrinogen hydrogels, Am. Chem. Soc. Biomater. Sci. Eng. 10 (2024) 6927–6937.

[20] Z. Feyissa, G.D. Edossa, N.K. Gupta, D. Negera, Development of double crosslinked sodium alginate/chitosan based hydrogels for controlled release of metronidazole and its antibacterial activity, Heliyon 9 (2023) e20144.

[21] J.E. Gough, C.A. Scotchford, S. Downes, Cytotoxicity of glutaraldehyde crosslinked collagen/poly(vinyl alcohol) films is by the mechanism of apoptosis, J. Biomed. Mater. Res. 61 (1) (2002) 121–130.

[22] J.-Y. Lai, Biocompatibility of genipin and glutaraldehyde cross-linked chitosan materials in the anterior chamber of the eye, Int. J. Mol. Sci. 13 (2012) 10970–10985.

[23] R.A.A. Muzzarelli, Genipin-crosslinked chitosan hydrogels as biomedical and pharmaceutical aids, Carbohydr. Polym. 77 (2009) 1–9.

[24] H. Cassimjee, P. Kumar, P. Ubanako, Y.E. Choonara, Genipin-crosslinked, proteosaccharide scaffolds for potential neural tissue engineering applications, Pharmaceutics 14 (2022) 441.

[25] J. Zvicer, V. Miskovic-Stankovic, B. Obradovic, Functional bioreactor characterization to assess potentials of nanocomposites based on different alginate types and silver nanoparticles for use as cartilage tissue implants, J. Biomed. Mater. Res. A 107A (2019) 755–768.

[26] J.P. Segovia-Gutiérrez, J.A. Rodríquez-Agudo, N. Binder, P.G. Weidler, F. Kirschhöfer, C. Fink-Straube, J. Utz, N. Germann, Dynamic mechanical analysis of alginate/gellan hydrogels under controlled conditions relevant to environmentally sensitive applications, Carbohydr. Polym. 352 (2025) 123180.

[27] D. Carmona-Cantillo, R. González-Cuello, R. Ortega-Toro, Comparative study between citric acid and glutaraldehyde in the crosslinking of gelatine hydrogels reinforced with cellulose nanocrystals (CNC), Gels 11 (2025) 790.

[28] M. Gil, I. Tiscornia, Ó. de la Iglesia, R. Mallada, J. Santamaría, Monoamine-grafted MCM-48: an efficient material for CO_2 removal at low partial pressures, Chem. Eng. J. 175 (2011) 291–297.

[29] S.L. Wingstrand, N.J. Alvarez, O. Hassager, J.M. Dealy, Oscillatory squeeze flow for the study of linear viscoelastic behaviour, J. Rheol. 60 (2016) 407–418.

[30] C. Dessi, Analysis of dynamic mechanical response in torsion, J. Rheol. 60 (2) (2016) 275–287.

[31] J. Diani, P. Gilormini, On necessary precautions when measuring solid polymer linear viscoelasticity with dynamic analysis in torsion, Polym. Test. 63 (2017) 275–280.

[32] D. Fauser, J.A. Rodríguez Agudo, H. Madadi, J. Haeberle, J. Renner, H. Steeb, Complex Poisson's ratio for viscoelastic materials: direct and indirect measurement methods and their correlation, Proc. R. Soc. A: Math. Phys. Eng. Sci. 481 (2309) (2025) 20240543.

[33] Y.S. Kim, J.A. Rodríguez-Agudo, M.P. Wistuba, J. Büchner, M. Schäffler, Determination of complex poisson's ratio of asphalt binders using torsion-tension tests in a dynamic shear rheometer, Road Mater. Pavement Des. 26 (2024) 397–419.

[34] M. Müller-Pabel, J.A. Rodríguez-Agudo, M. Gude, Measuring and understanding cure-dependent viscoelastic properties of epoxy resin: a review, Polym. Test. 114 (2022) 107701.

[35] J.A. Rodríguez-Agudo, J. Haeberle, M. Müller-Pabel, A. Troiss, A. Shetty, J. Kaschta, C. Giehl, Characterization of the temperature and frequency dependency of the complex poisson's ratio using a novel combined torsional-axial rheometer, J. Rheol. 67 (6) (2023) 1221–1250.

[36] C. Dessi, S. Coppola, D. Vlassopoulos, Dynamic mechanical analysis with torsional rectangular geometry: A critical assessment of constrained warping models, J. Rheol. 65 (3) (2021) 325–335.

[37] A. Vo, X. Feng, D. Patel, A. Mohammad, D. Kozak, S. Choi, M. Ashraf, X. Xu, Factors affecting the particle size distribution and rheology of brinzolamide ophthalmic suspensions, Int. J. Pharm. 586 (2020) 119495.

[38] Y. Bu, J. Liu, J. Fan, X. Chen, H. Yan, Q. Lin, Silica nanoparticle-reinforced bioactive oxidized alginate/polyacrylamide–gelatin interpenetrating polymer network composite hydrogels, Gels 11 (9) (2025) 748.

[39] E. Kontou, A. Chirstopoulos, P. Koralli, D.E. Mouzakis, The effect of silica particle size on the mechanical enhancement of polymer nanocomposites, Nanomaterials 13 (6) (2023) 1095.

[40] D.R. Hyden, C.L. Kennedy, K.P. Velikov, A. van Blaaderen, A. Imhof, Seeded-growth of silica rods from silica-coated particles, Langmuir 35 (2019) 14913–14919.

[41] A. Li, T. Gong, X. Yang, Y. Guo, Interpenetrating network gels with tunable physical properties: glucono-δ-lactone induced gelation of mixed Alg/gellan sol systems, Int. J. Biol. Macromol. 151 (2020) 257–267.

[42] R. Meera Naachiyar, M. Ragam, S. Selvasekarapandian, M. Vengadesh Krishna, P. Buvaneshwari, Development of biopolymer electrolyte membrane using Gellan gum biopolymer incorporated with NH4SCN for electro-chemical application, Ionics 27 (2021) 3415–3429.

[43] J. Galan, J. Trilleras, P.A. Zapata, V.A. Arana, C.D. Grande-Tovar, Optimization of chitosan glutaraldehyde-crosslinked beads for reactive blue 4 anionic dye removal using a surface response methodology, Life 11 (2) (2021) 85.

[44] J. Lewandowska-Łańcucka, A. Gilarska, A. Buła, W. Horak, A. Łatkiewicz, M. Nowakowska, Genipin crosslinked bioactive collagen/chitosan/hyaluronic acid injectable hydrogels structurally amended via covalent attachment of surface-modified silica particles, Int. J. Biol. Macromol. 136 (2019) 1196–1208.

[45] R.H. Ellerbrock, M. Stein, J. Schaller, Comparing silicon mineral species of different crystallinity using Fourier transform infrared spectroscopy, Front. Environ. Chem. 5 (2024) 1462678.

[46] M. Ulfa, D. Prasetyoko, W. Trisunaryanti, H. Bahruji, Z.A. Fadila, N.A. Sholeha, The effect of gelatin as pore expander in green synthesis mesoporous silica for methylene blue adsorption, Sci. Rep. 12 (2022) 15271.

[47] M.F. Butler, Y.-F. Ng, P.D.A. Pudney, Mechanism and kinetics of the crosslinking reaction between biopolymers containing primary amine groups and genipin, J. Polym. Sci. A Polym. Chem. 41 (2003) 3941–3953.

[48] C. Modrogan, A.M. Pandele, C. Bobirică, D. Dobrotă, A.M. Dăncilă, G. Gârleanu, D. Gârleanu, C. Orbeci, Synthesis, characterization and sorption capacity examination for novel hydrogel composite based on gellan gum and graphene oxide (GG/GO), Polymers 12 (2020) 1182.

[49] B. Sarker, D.G. Papageorgiou, R. Silva, T. Zehnder, F. Gul-E-Noor, M. Bertmer, A. R. Boccaccini, Fabrication of alginate-gelatin crosslinked hydrogel microcapsules and evaluation of the microstructure and physico-chemical properties, J. Mater. Chem. B 2 (2014) 1470–1482.

[50] A. Panday, H. Yadav, J. Patel, R. Paliwal, S. Maiti, Calcium silicate-reinforced pH-sensitive alginate-gellan gum composite hydrogels for prolonged drug delivery, J. Appl. Polym. Sci. 140 (2023) e54392.

[51] P. Wang, Z. Luo, Z. Xiao, Preparation, physicochemical characterization and in vitro release behavior of resveratrol-loaded oxidized gellan gum/resistant starch hydrogel beads, Carbohydr. Polym. 260 (2021) 117794.

[52] K. Bertula, L. Martikainen, P. Munne, S. Hietala, J. Klefström, O. Ikkala, Nonappa, Strain-stiffening of agarose gels, Am. Chem. Soc. Macro Lett. 8 (6) (2019) 670–675.

[53] A.J. Gravelle, S. Barbut, A.G. Marangoni, Influence of particle size and interfacial interactions on the physical and mechanical properties of particle-filled myofibrillar protein gels, R. Soc. Chem. Adv. 5 (2015) 60723–60735.

[54] K.L. White, S. Hawkins, M. Miyamoto, A. Takahara, H.-J. Sue, Effects of aspect ratio and concentration on rheology of epoxy suspensions containing model plate-like nanoparticles, Phys. Fluids 27 (2015) 123306.

[55] G. Zhang, Y. Zhou, Z. Ding, L. Fu, S. Wang, Nanosilica-supported thiosemicarbazide–glutaraldehyde polymer for selective Au(III) removal from aqueous solution, R. Soc. Chem. Adv. 7 (2017) 55215.

[56] J.Y. Ng, P. Yu, D.M. Murali, Y.-S. Liu, R. Gokhale, P.L.R. Ee, The influence of pregelatinized starch on rheology of a gellan-collagen IPN hydrogel for 3D bioprinting, Chem. Eng. Res. Des. 192 (2023) 477–486.

[57] A. Banerjee, S. Ganguly, Mechanical behaviour of alginate film with embedded voids under compression-decompression cycles, Sci. Rep. 9 (2019) 13193.

[58] Y. Zhang, Y. Zhang, L. Tang, Z. Liu, Z. Jiang, Y. Liu, L. Zhou, X. Zhou, Uniaxial compression constitutive equations for saturated hydrogel combined water-expelled behavior with environmental factors and the size effect, Mech. Adv. Mater. Struct. 29 (2022) 7491–7502.